ELSEVIER

Contents lists available at ScienceDirect

Scripta Materialia

journal homepage: www.elsevier.com/locate/scriptamat



Long-term tensile creep behavior of a family of FCC-structured multi-component equiatomic solid solution alloys



Di Xie^a, Rui Feng^a, Peter K. Liaw^a, Hongbin Bei^b, Yanfei Gao^{a,*}

- ^a Department of Materials Science and Engineering, University of Tennessee, Knoxville, TN 37996, USA
- ^b School of Materials Science and Engineering, Zhejiang University, Hangzhou 310058, PR China

ARTICLE INFO

Article history: Received 23 November 2021 Revised 20 January 2022 Accepted 21 January 2022

Keywords:
Creep deformation
Creep lifetime
Dislocation climb
Multicomponent equiatomic solid solution
alloy

ABSTRACT

Long-term tensile creep experiments were performed at 973 K on a family of multicomponent equiatomic solid solution alloys with face-centered cubic crystal structures, including quinary CoCrFeMnNi alloy and quaternary CoCrFeNi alloy, together with our previous report on ternary CoCrNi alloy. Analyzing the steady-state and transient creep properties and characterizing the precipitate evolution, it is suggested that dislocation creep be the dominant deformation mechanism for all these alloys. Although CoCrNi shows the highest room-temperature strength and the lowest creep rate at 973 K, the creep lifetime data for all three alloys are similar and can be described by the Monkman-Grant relationship.

© 2022 Acta Materialia Inc. Published by Elsevier Ltd. All rights reserved.

In the past two decades, multi-principal element alloys (MPEAs) have opened a wide range of opportunities in designing new alloys with desirable mechanical properties [1-4]. A well-investigated example among all MPEAs is the CrCoNi-based single-phase FCC alloys that have excellent strength and ductility combination from room temperature down to cryogenic temperatures [5,6]. Recently, more and more attention has been placed on the high-temperature performance of this class of MPEAs, due to the superior oxidation and corrosion resistance [7-9]. Many creep experiments on the CoCrFeMnNi have been reported. For example, Cao et al. [10] reported a stress-dependent transition of creep mechanism from dislocation climb mechanism in a low-stress region (LSR-region I) to a combined mechanism of dynamic recrystallization, precipitation, and dislocation climb in a high-stress region (HSR-region II) at a temperature range in a CoCrFeMnNi alloy from 773 to 873 K. Kang et al. [11] also reported the transition of creep mechanism from dislocation climb to glide in CoCrFeMnNi at a load range of 20-100 MPa. Rozman et al. [7] conducted a tensile creep test and reported a stress exponent of 6.2 which indicates dislocation creep as the rate-controlling mechanism, but the above-mentioned transition in [10,11] was not observed. Moreover, a much lower stress exponent of \sim 3.7 is reported by Zhang et al. [8] by conducting the tensile creep in a vacuum environment from 1023 to 1073 K. It should be pointed out that tests of CoCrFeMnNi at 273 and 77 K also give a wide range of strength and ductility values from various groups, most likely due to the processing conditions and microstructural differences in these tests. The research focus is therefore suggested to be placed on a comparative study of CoCrFeMnNi and subset alloys. Along this line, our previous study in [5] has found the strongest solid-solution strengthening in CoCrNi, followed by a few quarternary subsets, and then by the quinary CoCrFeMnNi, although the corresponding activation volumes are similar (10–20 b^3 at 77 K and 50–80 b^3 at 293 K, with b being the Burgers vector). The strength measurements have been extended to high temperatures, but the creep properties of all these CoCrFeMnNi and subset alloys have not been systematically investigated. Such a comparative study will further our understanding of the synergistic roles of solid solution strengthening and high-temperature creep mechanisms.

In this work, the tensile creep behaviors of CoCrFeMnNi and CoCrFeNi at 973 K are carefully investigated, complemented by our previous report on CoCrNi at 973, 1023, and 1073 K [12]. Through comparison of the creep performance of the CoCrFeMnNi, CoCrFeNi, and CoCrNi, this study can shed light on designing strategies for novel materials for high-temperature applications. To ensure consistency, CoCrFeNi and CoCrFeMnNi, together with the previously studied CoCrNi, were fabricated together by arc-melting, remelting, drop-casting, and cold rolling. All the elements were remelted five times, drop-cast into a copper mold with a dimension of 12.7 mm \times 25.4 mm \times 127 mm, and then homogenized for 24 h at 1473 K and water quenching. After that, these materials were cold-rolled along the longitudinal ingot direction to a total thickness reduction of 90–92% without cross-rolling or intermediate an-

^{*} Corresponding author. E-mail address: ygao7@utk.edu (Y. Gao).

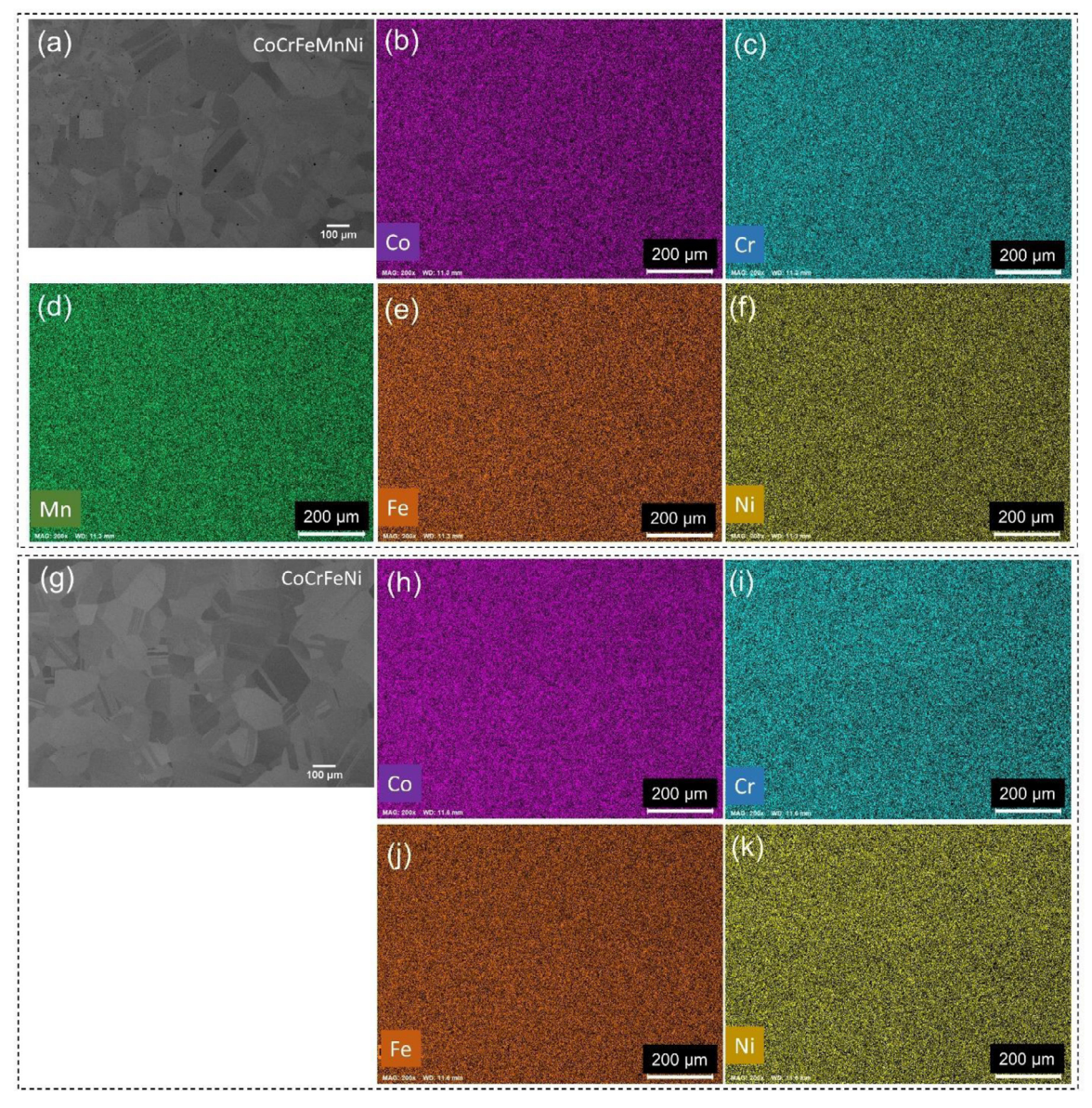


Fig. 1. (a) BSE-SEM image, and (b-f) the corresponding EDS elemental maps for CoCrFeMnNi after annealing at 1100 °C for 1 h; (g) SEM image, and (h-k) corresponding EDS elemental maps for CoCrFeNi after annealing at 1100 °C for 1 h.

nealing. Dog-bone cylindrical specimens with gage dimensions of $\phi 3.175~{\rm mm} \times 28~{\rm mm}$ were cut from the cold rolling sheets by electrical discharge machining (EDM) with longitudinal axes parallel to the rolling direction, sealed in vacuum-quartz tubes, and subsequently annealed at 1373 K for 2 h or 1 h to remove the deformation substructure from cold rolling and achieve similar grain size. The gage sections of the samples were mechanically polished using 800-grit SiC paper before the mechanical test. Tensile creep tests were performed on these samples under constant load mode at 973 K.

Scanning electron microscopy (SEM) was conducted on a Zeiss EVO SEM to investigate the grain characteristics of CoCrFeMnNi, and CoCrFeNi. The initial grain size was measured by the line intercept method on the backscattered electron (BSE) SEM images and at least 150 grains were counted for each specimen. The distribution of alloying elements after fracture was then characterized by energy dispersive spectroscopy (EDS) maps. The microstructures of the creep specimens prior to testing are shown in Fig. 1, where the grains are fully recrystallized and equiaxed after the annealing treatment with an average size range of 140–150 μ m, and

the alloying elements distribute uniformly in the matrix. Transmission electron microscopy (TEM) characterization was performed on ZEISS LIBRA 200 HT FE MC. Thin foils for the TEM observations were taken from the gage section of crept/ruptured samples. The TEM thin foils were prepared by twin-jet polishing, using an electrolyte consisting of 95% (volume percent) ethanol and 5% perchloric acid in a volume fraction at a temperature of -40 °C and an applied voltage of 30 V.

Representative creep curves obtained from the creep experiments under 973 K on CoCrFeMnNi, CoCrFeNi, and CoCrNi [12] at 70 MPa are shown in Fig. 2(a). It is interesting to see that the classic primary, secondary and tertiary regions can be observed in CoCrFeNi and CoCrNi, but there is an "inverted" primary creep in CoCrFeMnNi, i.e., the creep rate first decreases then increases to its steady-state value. A similar observation was reported recently in CoCrFeMnNi [8]. The primary creep is controlled by the competition between work hardening and recovery. The formation of normal primary creep region that is observed in CoCrFeNi, and CoCrNi is related to the decrease in mobile dislocation density in pure metals and class M alloys, where subgrain boundaries are typically

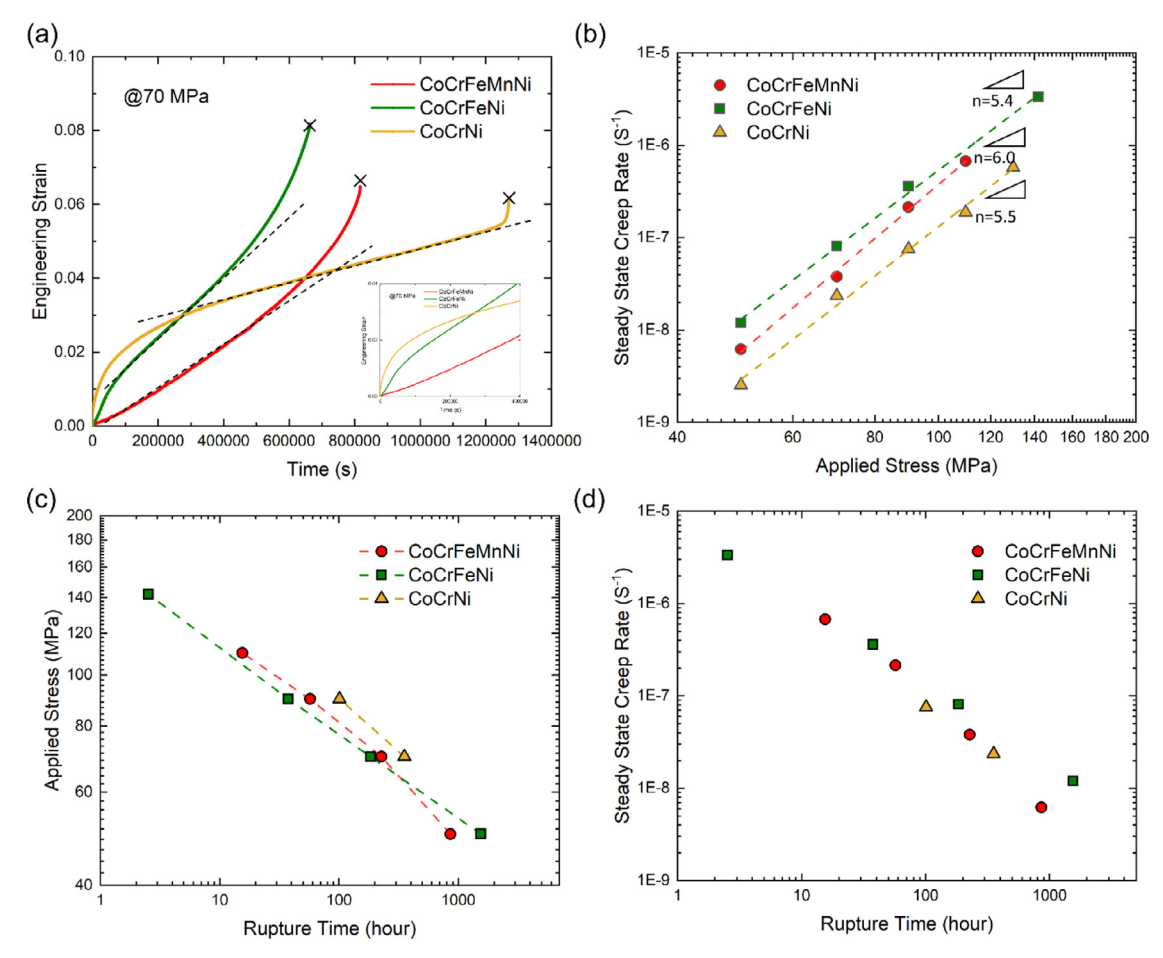


Fig. 2. (a) Selected creep strain-time curves at 70 MPa for CoCrFeMnNi, CoCrFeNi, CoCrNi [12], (b) Dependence of the steady-state strain rate on the applied stress on a double logarithmic scale, (c) A plot of the applied stress versus time to rupture time, and (d) A plot of the creep strain rate to rupture time.

formed [13]. The primary creep of CrMnFeCoNi behaves like conventional class A alloys (i.e., Al-Mg alloys) that show an "inverted" primary creep, where the creep rate accelerates to a steady state by the increase of mobile dislocation density under stress typically without the formation of subgrains [14].

The dependence of the steady-state strain rate $\dot{\varepsilon}_{SS}$ of CoCr-FeMnNi, CoCrFeNi, and CoCrNi [12] on the applied stress σ on a double logarithmic scale is given in Fig. 2(b), where the largest steady-state strain rate is observed in CoCrFeNi, and the smallest one in the CoCrNi at the same load level. The relationship between steady-state creep rate, $\dot{\varepsilon}_{SS}$, and applied stress, σ , follows empirical power-law equation [15]:

$$\dot{\varepsilon}_{ss} = A_n \sigma^n \exp\left(-\frac{Q}{RT}\right) \tag{1}$$

where A_n is a material constant, n is the stress exponent, Q is the apparent activation energy, R is the gas constant, and T is the absolute temperature. Consistent stress exponents, n, are obtained by fitting the relationship between $\dot{\varepsilon}_{\rm SS}$, and σ , leading to 6.0 ± 0.2 for CoCrFeMnNi and 5.4 ± 0.1 for CoCrFeNi at 973 K. The fitted stress exponent value in this work together with stress value for CoCrNi from our previous work are summarized in Table 1. These n values are in the common range of the stress exponent (4–7) for dislocation climb-controlled creep [16]. There are no deformation mechanism transitions in these alloys under the current temperature and load range in this study.

Creep lifetime, $t_{\rm r}$, with the applied stress at 973 K for CoCr-FeMnNi, CoCrFeNi, and CoCrNi [12] has been plotted in Fig. 2(c) and (d). The relationship between creep rupture time and mini-

Table 1 The fitted stress exponent n, activation volume ΔV^* , and lattice constant a for the CoCrFeMnNi, CoCrFeNi, and CoCrNi [12] at 973 K.

	n	$\Delta V^* (nm^3)$		a (Å)
CrMnFeCoNi	6.0	0.184 (nm³)	112 b ³	3.5991
CoCrFeNi	5.4	0.199 (nm³)	123 b ³	3.5715
CoCrNi	5.5	0.140 (nm³)	88 b ³	3.5590

mum creep rate follows the empirical Monkman–Grant relationship as $\dot{\varepsilon}_{\rm SS}t_{\rm r}=C$, where C is constant [17]. We can see the CoCrNi exhibits the greatest creep lifetime, followed by the CoCrFeMnNi, and then CoCrFeNi under the same stress level. However, the corresponding strain rate for CoCrNi is the lowest, and the resulting Monkman–Grant constant C is rather similar for all these three alloys. The final fracture strain, which is larger than C as C only contains the steady–state strain level, is comparable to many commercial ferritic steels (e.g., P92 and P122) although the latter are usually consisting of complex lath–martensite microstructures while all our alloys here are single–phase solid solution.

The standard model for the thermally activated process is given by the following equation [18]:

$$\dot{\varepsilon} = \dot{\varepsilon}_0 \exp\left(-\frac{\Delta G}{k_B T}\right) = \dot{\varepsilon}_0 \exp\left(-\frac{\Delta F}{k_B T} + \frac{\sigma \Delta V^*}{\sqrt{3} k_B T}\right)$$
 (2)

where ΔG is the activation energy, ΔF is the activation enthalpy, k_B is the Boltzmann constant, and ΔV^* is the activation volume. The factor $\sqrt{3}$ is introduced for the conversion between normal

Table 2 A comparison of creep experiments for CrCoNi-based alloys.

Alloys	Test Method	n	V (b ³)	Q (kJ/mol)	T range (K)	Stress Range (MPa)	Mechanism	Sample Geometry (mm)	Refs.
CoCrFeMnNi	Compressive, stepwise loading	6.3	300-800	246 (973–1023 K) or 704 (1023–1073 K)	973–1023 1023–1073	10-100	Dislocation motion	Cylindrical bar 12(L) × Φ5	Dobeš et al. [20]
	Strain rate jump	$<=3 (low \dot{\varepsilon})$ 5(high $\dot{\varepsilon}$)	67.6–123.6 (low $\dot{\varepsilon}$) 38.3–68.5 (high $\dot{\varepsilon}$)	$280(\text{low } \dot{\varepsilon})$ $330(\text{high } \dot{\varepsilon})$	1023-1123	7–260	Dislocation glide (low $\dot{\varepsilon}$)) Dislocation climb (high $\dot{\varepsilon}$)	$\begin{array}{l} \text{Flat sheet} \\ 12(\text{L}) \times 4(\text{W}) \\ \times \ 1.3(\text{H}) \end{array}$	He et al. [21]
	Tensile creep	5–6 (low <i>σ</i>) 8.9–14 (high <i>σ</i>)	-	268 (low σ) 380 (high σ)	773–873	140-400	Dislocation climb/ dynamic recrystallization, precipitation, and dislocation climb	Flat sheet $25(L) \times 5.6(W) \times 1.5(H)$	Cao et al. [10]
Tensile cree	Tensile creep	~3 ~6	-	305-319 236-249	808-923	20-100	Dislocation creep Dislocation glide	Flat sheet $9(L) \times 1(H)$	Kang et al. [11]
	Tensile creep	~ 3.7	-	~230	1023-1173	20–200	dislocation- dislocation interactions and dislocation-lattice interactions	Flat sheet 35.56(L) × 2.54(W) × 1(H)	Zhang et al. [8]
	Tensile creep	~ 6.2	-	394	848 -923	103-207	Dislocation creep	Cylindrical bar $31.75(L) \times \Phi6.25$	Rozman et al.
	Tensile creep	6.0	112	-	973	50-110	Dislocation creep	Cylindrical bar 28(L) × Φ3.175	This work
CoCrFeNi	Tensile creep	5.4	123	-	973	50-142	Dislocation creep	Cylindrical bar 28(L) × Φ3.175	This work
CoCrNi	Tensile creep	5.5	88	370	973-1073	50–130	Dislocation creep	Cylindrical bar $28(L) \times \Phi 3.175$	Xie et al. [12]

and shear strengths. Eq. (2) can be converted into Eq. (3) to evaluate the activation volume, ΔV^* , for CoCrFeMnNi, CoCrFeNi, CoCrNi:

$$\Delta V^* = \sqrt{3}kT \left(\frac{\partial ln\dot{\varepsilon}_{ss}}{\partial \sigma} \right) \tag{3}$$

From the above equation, the creep test results can be used to determine the activation volume. The thermal parameters derived from the current creep tests for these alloys and lattice constant for these alloys are also summarized in Table 1. We notice that the magnitudes of the activation volume of CoCrNi [12], CoCr-FeNi, and CoCrFeMnNi at 973 K are in the range of 80 \sim 130 b^3 , where b = (a/2 < 110 >) is the Burgers vector. The quaternary alloy, CoCrFeNi, exhibits the largest activation volume value, the ternary alloy, CoCrNi, shows the smallest one, and the quinary allov. CoCrFeMnNi, gives the intermediate one. The higher V* indicates a larger volume of atoms contributing to the thermal activation process during creep, which will result in a greater creep rate in CoCrFeNi. For comparison, the corresponding activation volumes of CoCrNi, CoCrFeNi, and CoCrFeMnNi are 13.5, 11.5, and 7.25b³ at 77 K, and 46.6, 61.6, 76.8b3 at 293 K from our previous work [5]. According to the typical range for forest dislocation hardening in FCC materials (several hundreds of b³) [19], these activation volumes suggest the specific thermally activated motion of dislocation, which further verifies the dislocation-mediated mechanism during the creep deformation of the CoCrFeMnNi, CoCrFeNi, and CoCrNi.

A comparison of the essential creep parameters between our study and previous studies is included in Table 2. It is interesting to note that although dislocation motion is the general dominant deformation mechanism for CoCrFeMnNi, there exists a discrepancy in the stress exponent values when compared with previous studies performed at comparable temperatures and load levels. It is worth noting that the dislocation-controlled creep, where dislocations glide, cross slip, and climb are operative dislocation mechanisms, is independent of grain size. Therefore, the differ-

ence in the grain size in these studies will not prevent comparing their creep properties. Dobeš et al. [20] conducted a compressive stepwise loading test and found a stress exponent of \sim 6.3 for CoCrFeMnNi. Rozman et al. [7] also reported a stress exponent of \sim 6.2 for CoCrFeMnNi in a tensile creep test. Both stress exponent values for CoCrFeMnNi are in good agreement with this research. However, a transition from glide control to dislocation climb control is reported by He et al. [21] using the strain rate jump test. Kang et al. [11] discovered the transition from dislocation climb to viscous glide by conducting high-temperature tensile creep tests. Zhang et al. [8] reported a uniform stress value of 3.7 for CoCr-FeMnNi and proposed that the value discrepancy can be related to the load history and oxygen effect during the strain/stress jump test. Interestingly, all CoCrFeMnNi specimens with cylinder geometry in the above studies exhibit a relatively large stress exponent value (\sim 6), while the specimens with flat geometry usually show a relatively small n value or deformation mechanism transition.

To further confirm the deformation mechanism, the microstructures in the crept specimens for CoCrFeNi, and CoCrFeMnNi under 70 MPa at 973 K have been investigated, as shown in Fig. 3. Clear evidence of redistribution of the constituent elements in these two specimens is presented in the BSE-SEM images, where chrome enriched phases tend to form primarily along grain boundaries. The bright-field (BF) TEM image of the precipitate in CoCrFeMnNi is exhibited in Fig. 4(a). Selected area electron diffraction (SAED) patterns are given in Fig. 4(b) to identify the precipitations in CoCr-FeMnNi. Similar to the precipitate type in the crept CoCrNi sample [12], Cr-rich tetragonal σ phase is identified according to the SAED patterns of FCC matrix and Cr-rich precipitate along the [110] zone axis. Unfortunately, we did not observe the precipitates in the prepared TEM sample for the CoCrFeNi, due to the localized observation nature of TEM analysis. It is yet reasonable to anticipate the precipitates in CoCrFeNi are also σ -type precipitates. The dislocation substructures for CoCrFeMnNi and CoCrFeNi have been examined by TEM, as shown in Fig. 4(c) and (d), respectively. In general, a large number of dislocations have accumulated and en-

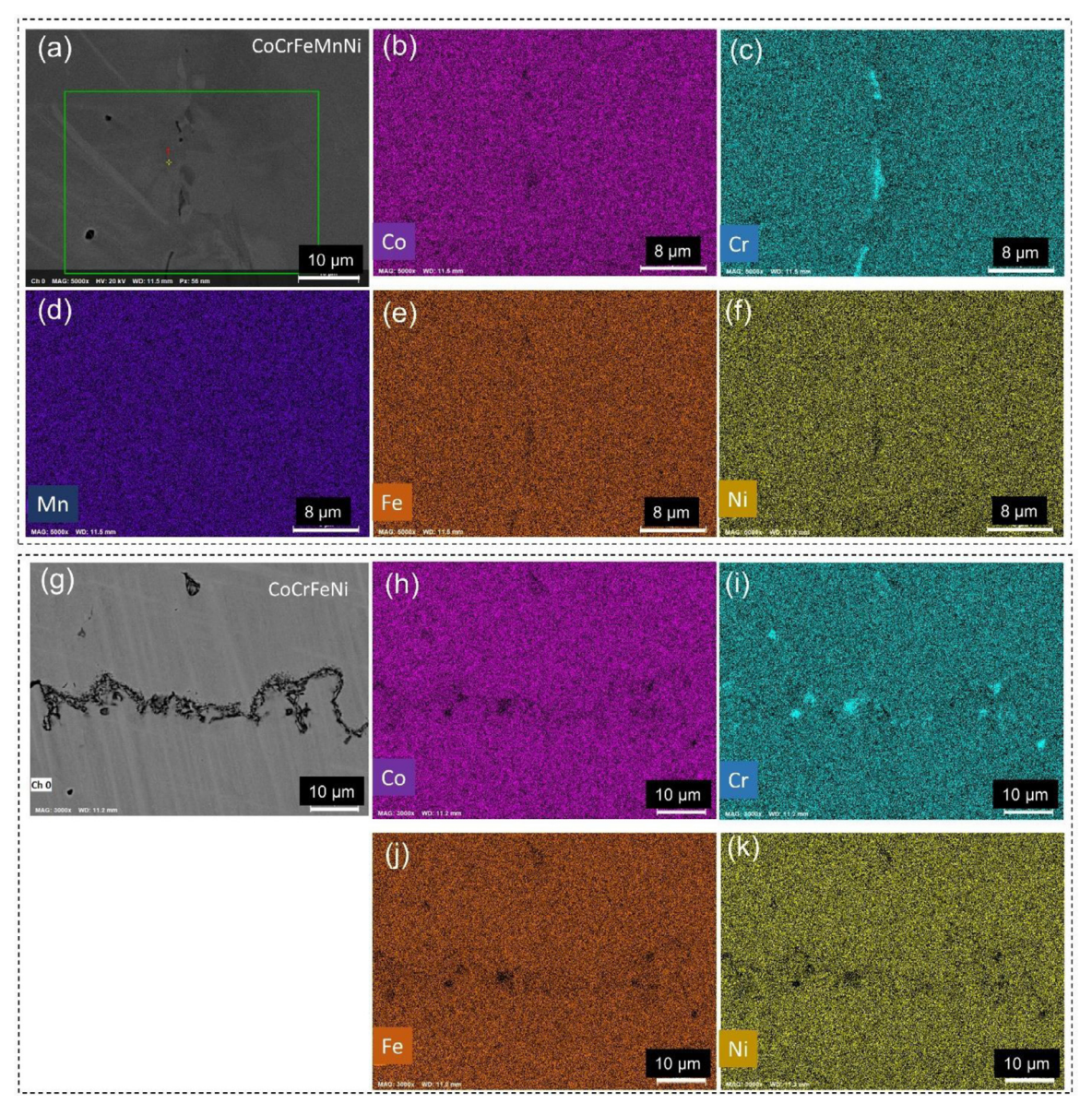


Fig. 3. (a) BSE-SEM image, and (b-f) the corresponding EDS elemental maps for CoCrFeMnNi after creep test (973 K, 70 MPa); (g) BSE-SEM image, and (h-k) the corresponding EDS elemental maps for CoCrFeNi after creep test (973 K, 70 MPa).

tangled with each other to form an uneven distribution in the CoCrFeMnNi and CoCrFeNi. The entangled dislocation configuration suggests a great extent of dislocation-dislocation interaction. The observed jog configurations, labeled by arrows, are indicative of a dislocation climb process, and thus the stress-assisted dislocation climbing process, as controlled by lattice diffusion, may be the operative creep mechanism of these alloys.

It is interesting to note that creep resistance order at the same stress magnitude is CoCrNi > CoCrFeMnNi > CoCrFeNi, while the yield strength order at room and cryogenic temperatures is CoCrNi > CoCrFeNi >> CoCrFeMnNi (after excluding contributions from Hall-Petch and other mechanisms than solid solution effects). CoCrFeNi and CoCrNi are subsets of CoCrFeMnNi, so what are the factors for the difference in the creep resistance in these alloys? The constitutive equation for climb-controlled dislocation creep with the stacking fault energy effect is given in the following form [22]:

$$\dot{\varepsilon}_{ss} = A \left(\frac{\gamma}{Gb}\right)^3 \left(\frac{Gb}{kT}\right) \left(\frac{\sigma}{G}\right)^5 D_L \tag{4}$$

where D_L is the lattice diffusion coefficient or pipe diffusion coefficient, γ is the stacking fault energy, G is the shear modulus, and A is a constant. Stacking fault energy (SFE) is one of the important parameters that determine the degree of recovery by affecting the extent to which dislocations dissociate, which in turn determines the rate of dislocation climb and cross slip. Apparently, low stacking-fault energy is advantageous for high creep resistance. Liu et al. [23] have reported an SFE value of 18 ± 4 mJ/m² of CoCrNi, 27 \pm 4 mJ/m² of CoCrFeNi, and 26.5 \pm 4.5 mJ/m² of CoCr-FeMnNi by weak-beam dark-field TEM at 293 K. The same measurement method has been taken by Laplanche et al. [24] to measure the stacking-fault energy of CoCrNi (22 \pm 4 mJ/m²) that is a quarter lower than that of CoCrFeMnNi (30 \pm 5 mJ/m²) [25]. Zaddach et al. [26] reported the SFE for equiatomic CoCrFeMnNi is in the range of 20-25 mJ/m² measured and the SFE for CoCrFeNi has been estimated to be $\sim 30 \text{ mJ/m}^2$ using X-ray diffraction and first-principles calculations. Recently, it has been reported a value of 16.1 mJ/m² [27] of CoCrNi, 32.1 mJ/m² [27] and 32.5 mJ/m² [28] of the CoCrFeNi at 293 K by neutron diffraction peak pro-

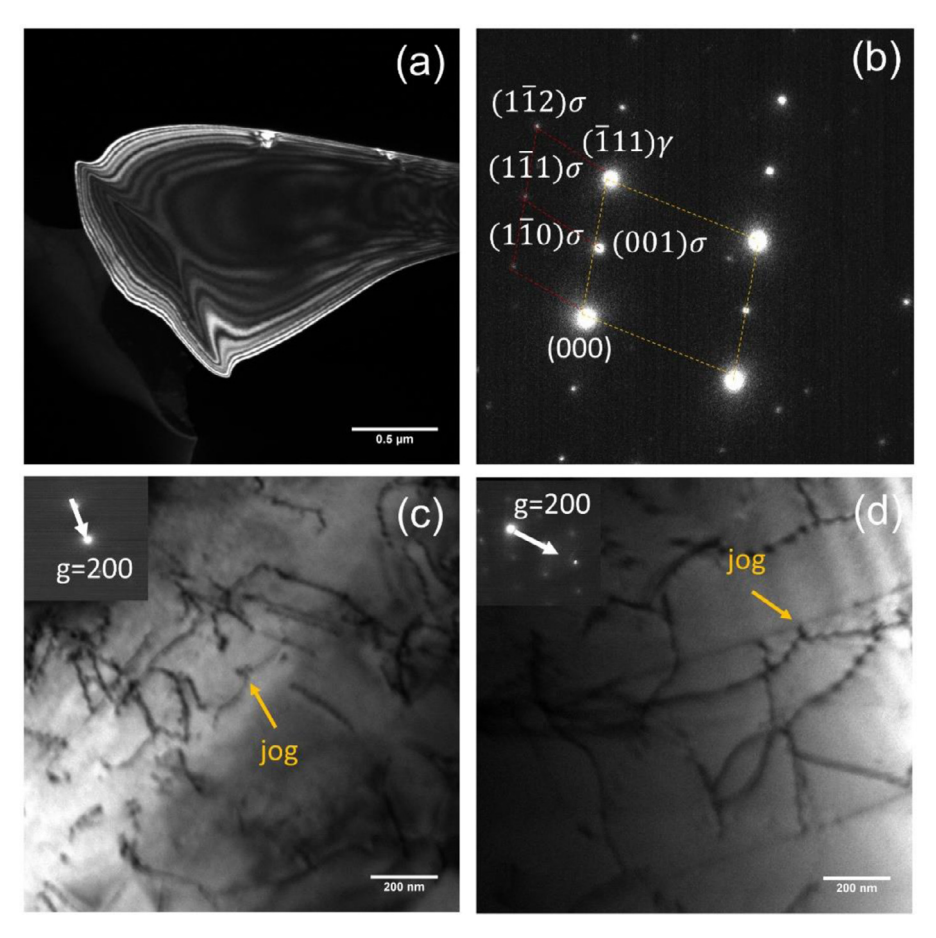


Fig. 4. (a) Bright-field (BF) image of the Cr-rich precipitate in CrCrFeMnNi, and (b) selected area electron diffraction (SAED) pattern along the [110] zone axis, (c) and (d) TEM images of dislocation substructures for CoCrFeMnNi and CoCrFeNi, respectively.

file analysis. Although the TEM-based SFE analysis has uncertainties caused by localized investigation, in general, the SFE of CoCrNi, CoCrFeNi, and CoCrFeMnNi at room temperature increase in the order: CoCrNi < CoCrFeMnNi < CoCrFeNi. It is known that the SFE will increase as the temperature increases as shown in [29]. Furthermore, Ref. [29] delineated the varying degrees of contributions from magenatic and chemical factors to the SFE's temperature dependence in twinning-induced plasiticty (TWIP) steels. The vibrational entropy is believed to be dominant in ab initio studies of various HEAs derived from the Cantor alloy [30], which also reports the linear dependence of SFE values in a temperature range from about 100 to 1000 K. Their calculations show the same order as the above limited measurements, i.e., CoCrNi < CoCrFeMnNi < CoCrFeNi, although the middle one gradually approaches the third. In alloys or metals with low SFE such as copper, climb is difficult, which slows down the dislocation-dominated creep. The SFE order is opposite to the trend of creep resistance. Based on Eq. (4), the relative decrease of the stacking fault energy may partly explain why CoCrNi shows a much better creep property than CoCrFeMnNi.

In summary, the tensile creep test has been performed on CoCrFeNi, and CoCrFeMnNi at 973 K, which yield a consistent stress exponent (~5.4 for CoCrFeNi, ~6.0 for CoCrFeMnNi) with no transition of rate-controlling creep mechanisms under the current load range. Dislocation climb mechanism is proposed to be the dominant deformation mechanism for both of the alloys. Comparing the creep properties of a family of equiatomic solid solution alloys (CoCrNi, CoCrFeNi, and CoCrFeMnNi) at 973 K, CoCrNi exhibits the greatest creep resistance and lifetime, and CoCrFeNi displays the least creep retardation and lifetime under the same load level,

which may be related to the difference in the stacking fault energies in these alloys. In contrast, the yield strengths of these materials at room and cryogenic temperatures have a different order than the above, mainly because the strengthening arises from mismatches in solid solution and many literature experiments do not exclude other non-solution effects completely or appropriately.

Declaration of Competing Interest

The authors declare that they have no known competing financial interests or personal relationships that could have appeared to influence the work reported in this paper.

CRediT authorship contribution statement

Di Xie: Conceptualization, Methodology, Writing – original draft. **Rui Feng:** Conceptualization, Methodology, Writing – original draft. **Peter K. Liaw:** Conceptualization, Methodology, Writing – original draft. **Hongbin Bei:** Conceptualization, Methodology, Writing – original draft. **Yanfei Gao:** Conceptualization, Methodology, Writing – original draft.

Data availability

Data contained in this paper are available upon request to the corresponding author.

Acknowledgments

DX and YG are grateful for the support from the US National Science Foundation (DMR 1809640), and HB to the internal fund-

ing from the School of Materials Science and Engineering, Zhejiang University.

References

- [1] D.B. Miracle, O.N. Senkov, Acta Mater. 122 (2017) 448-511.
- [2] Y.F. Ye, Q. Wang, J. Lu, C.T. Liu, Y. Yang, Mater. Today 19 (6) (2016) 349-362.
- [3] O.N. Senkov, J.D. Miller, D.B. Miracle, C. Woodward, Nat. Commun. 6 (2015) 6529.
- [4] W. Li, D. Xie, D. Li, Y. Zhang, Y. Gao, P.K. Liaw, Prog. Mater. Sci. 118 (2021) 100777.
- [5] Z. Wu, Y. Gao, H. Bei, Acta Mater 120 (2016) 108–119.
- [6] Z. Wu, H. Bei, F. Otto, G.M. Pharr, E.P. George, Intermetallics 46 (2014) 131-140.
- [7] K.A. Rozman, M. Detrois, T. Liu, M.C. Gao, P.D. Jablonski, J.A. Hawk, J. Mater. Eng. Perform. 29 (9) (2020) 5822-5839.
- [8] M. Zhang, E.P. George, J.C. Gibeling, Scr. Mater. 194 (2021) 113633.
- [9] T. Cao, J. Shang, J. Zhao, C. Cheng, R. Wang, H. Wang, Mater. Lett. 164 (2016) 344-347.
- [10] C. Cao, J. Fu, T. Tong, Y. Hao, P. Gu, H. Hao, L. Peng, Entropy 20 (12) (2018) 960.
- [11] Y.B. Kang, S.H. Shim, K.H. Lee, S.I. Hong, Mater. Res. Lett. 6 (12) (2018) 689-695
- [12] D. Xie, R. Feng, P.K. Liaw, H. Bei, Y. Gao, Intermetallics 121 (2020) 106775.
 [13] P. Yavari, F.A. Mohamed, T.G. Langdon, Acta Metall. 29 (8) (1981) 1495–1507.
- [14] F.A. Mohamed, T.G. Langdon, Acta Metall. 22 (6) (1974) 779–788.

- [15] A.K. Mukherjee, J.E. Bird, J.E. Dorn, Experimental Correlations For High-Temperature Creep, Lawrence Berkeley National Laboratory, 1968 Report at.
- [16] M.A. Meyers, K.K. Chawla, Mechanical Behavior of Materials, Cambridge University Press, 2008.
- [17] F.C. Monkman, Proc. ASTM (1956) 91-103.
- [18] D. Caillard, J.L. Martin, Thermally Activated Mechanisms in Crystal Plasticity, Pergamon, 2003.
- [19] H. Conrad, Mater. Sci. Eng. A 341 (1-2) (2003) 216-228.
- [20] F. Dobeš, H. Hadraba, Z. Chlup, A. Dlouhý, M. Vilémová, J. Matějíček, Mater. Sci. Eng. A 732 (2018) 99–104.
- [21] J.Y. He, C. Zhu, D.Q. Zhou, W.H. Liu, T.G. Nieh, Z.P. Lu, Intermetallics 55 (2014) 9-14.
- [22] B.J. Burton, Acta Metall. 30 (5) (1982) 905–910.
- [23] S.F. Liu, Y. Wu, H.T. Wang, J.Y. He, J.B. Liu, C.X. Chen, X.J. Liu, H. Wang, Z.P. Lu, Intermetallics 93 (2018) 269–273.
- [24] G. Laplanche, A. Kostka, C. Reinhart, J. Hunfeld, G. Eggeler, E.P. George, Acta Mater. 128 (2017) 292-303.
- [25] N.L. Okamoto, S. Fujimoto, Y. Kambara, M. Kawamura, Z.M. Chen, H. Matsunoshita, K. Tanaka, H. Inui, E.P. George, Sci. Rep. 6 (2016) 35863.
- [26] A.J. Zaddach, C. Niu, C.C. Koch, D.L. Irving, JOM. 65 (12) (2013) 1780–1789.
- [27] W. Woo, M. Naeem, J.S. Jeong, C.M. Lee, S. Harjo, T. Kawasaki, H. He, X.L. Wang, Mater. Sci. Eng. A 781 (2020) 139224.
- [28] Y. Wang, B. Liu, K. Yan, M. Wang, S. Kabra, Y.L. Chiu, D. Dye, P.D. Lee, Y. Liu, B. Cai, Acta Mater. 154 (2018) 79-89.
- [29] S. Curtze, V.T. Kuokkala, Acta Mater. 58 (15) (2010) 5129-5141.
- [30] S. Zhao, G.M. Stocks, Y. Zhang, Acta Mater. 134 (2017) 234-345.